ACI STRUCTURAL JOURNAL TECHNICAL PAPER

Title No. 120-S76

Behavior of NiTi Shape Memory Alloy- and Steel-Reinforced Shear Walls Repaired with Engineered Cementitious Composite

by Michael A. Soto-Rojas, Anca C. Ferche, and Dan Palermo

This paper presents the results of an experimental study investigating the response of two shear walls repaired with engineered cementitious composite (ECC). One of the walls was reinforced in the boundary regions within the plastic hinge with superelastic, nickel-titanium (NiTi) shape memory alloy (SMA) bars, while the companion wall was reinforced with deformed mild steel bars only. The repair method involved the removal of the heavily damaged concrete in the plastic hinge zone, replacement of ruptured and buckled steel reinforcement, placement of starter bars at the base of the walls, and casting of ECC to replace the removed concrete. The SMA bars were reused as they sustained no damage from the initial testing. Summarized in this paper are an assessment of the performance of the repaired walls and a comparison with the responses of the walls previously tested in their original condition. The experimental program highlights the enhanced performance of the composite system that integrates the self-centering capabilities of SMA bars and the distinctive tension strain hardening and ductility of ECC. The lateral strength was markedly increased, while the energy dissipation and recovery capacities, in general, were improved for the repaired walls compared to the original walls. The repaired steel-reinforced wall developed a peak lateral strength of 23% larger compared to the original wall, while the repaired SMA-reinforced wall had a 16% increase in peak lateral strength compared to the original specimen. The strength enhancement of the repaired walls led to higher dissipated energy throughout testing. For both sets of walls, the SMA-reinforced walls exhibited larger rotations compared to the steel-reinforced walls primarily on account of the lower stiffness of the SMA bars.

Keywords: energy dissipation; engineered cementitious composite (ECC); nickel-titanium (NiTi); recovery capacity; reinforced concrete; repair; shape memory alloys (SMAs); shear walls.

INTRODUCTION

Reinforced concrete structures designated as normal importance are designed to behave in the inelastic range during rare events such as high seismic loading, the primary objective being safeguarding against collapse and ensuring life safety. This is achieved through the design of plastic hinge regions that are controlled by the yielding of the reinforcement, resulting in significant residual deformations and damage.[1-3] Structures built in the major cities of Chile were designed based on relatively current codes,[4] and they experienced severe permanent damage during the 2010 earthquake.[5] A similar scenario occurred in Christchurch, New Zealand, during the 2011 earthquake.[6] This resulted in compromised, post-earthquake infrastructure in terms of structural integrity and functionality, leading to significant economic deficits.

The owners of structures damaged during design-level seismic events typically have two alternatives: demolition and replacement; or repair to recover the strength, stiffness, and ductility of the structure. The first alternative is highly disruptive and expensive, impacting the affected community for a significant period. The second alternative has the potential to be more desirable when the extent of damage is limited, and the repair operations are feasible and can be executed in a reasonable time frame.

Ductility capacity and energy dissipation are two primary characteristics well-designed reinforced concrete structures are expected to exhibit. In addition, ease of repair after rare loading events is preferable from a reliability perspective. The implementation of innovative materials such as shape memory alloy (SMA) bars and engineered cementitious composite (ECC) materials provide an opportunity to improve the post-earthquake state of structures while achieving the primary design objectives of preventing collapse and safeguarding against loss of life. By limiting the post-earthquake residual damage, demolition may be avoided, and repairs for a relatively immediate occupancy become possible. The combination of these two materials leads to self-centering behavior with improved damage tolerance.

Applications of SMAs in structural systems have received increased research focus during the past decade as a viable option to design resilient structures. The recentering ability of SMAs makes them attractive for structures expected to experience large deformations. SMAs dissipate energy through hysteretic damping and can reach strengths comparable to mild steel reinforcing bars. Disadvantages of SMA bars include high initial cost, smooth surface, low elastic modulus, and the need for couplers to connect with conventional bars. The most common type of SMA studied for structural applications, which was also used for this experimental program, is a nickel-titanium (NiTi) alloy consisting of approximately 56% nickel and 44% titanium. ECC materials are a special class of high-performance fiber-reinforced cement composites and consist typically of a mortar base

ACI Structural Journal, V. 120, No. 4, July 2023.

MS No. S-2022-238.R2, doi: 10.14359/51738745, received January 9, 2023, and reviewed under Institute publication policies.

matrix comprising sand, silica fume, cement, fly ash, and up to a 2% volumetric fraction of polyvinyl alcohol (PVA) fibers.[7,8] The tensile capacity varies between 4 and 6 MPa, and the response exhibits high ductility.

Experimental investigations on the use of SMA bars in concrete elements for new design and for the repair of concrete elements are limited and consist of applications for columns, beam-columns joints, beams, and shear walls.[9-17] Abdulridha and Palermo[9] and Morcos and Palermo[10,11] illustrated that substituting deformed longitudinal reinforcement with SMA bars in the boundary regions within the plastic hinge of a slender shear wall results in greater recentering capacity and reduced residual displacements. Cortés-Puentes et al.[12] repaired a previously tested SMA-reinforced shear wall by replacing the damaged reinforcing bars within the plastic hinge region with new segments and the damaged concrete with self-consolidating concrete (SCC). The response of the repaired wall under cyclic loading was comparable to its response in the original state in terms of strength, stiffness, and cracking pattern. Saiidi et al.[13] demonstrated substantial benefits such as self-centering and improved damage tolerance when using a combination of SMA longitudinal bars and ECC in the plastic hinge region of a column.

RESEARCH SIGNIFICANCE

The experimental study presented herein focused on the structural behavior of a composite system that integrates NiTi SMA, mild steel bars, and ECC to enhance the performance of a shear wall subjected to reversed cyclic loading. The investigation studied the applicability of ECC as part of a repair method for heavily damaged SMA- and steel-reinforced concrete shear walls that were previously tested. This study highlights the benefits of implementing ECC concrete and SMA reinforcement to enhance the post-repair behavior under simulated seismic loading by reducing the permanent deformation and damage typically experienced by shear walls. To the best of the authors' knowledge, this is the first study to test a hybrid SMA-steel-reinforced shear wall repaired with ECC. The results of this study will be of general interest to practicing structural engineers and standards committees, with the goal of accelerating the acceptance of high-performance design concepts and repair strategies incorporating NiTi SMA bars and ECC.

EXPERIMENTAL PROGRAM

The shear walls investigated in this study were previously tested by Morcos and Palermo[10] under a reversed cyclic lateral loading protocol. The experimental program undertaken by Morcos and Palermo[10] focused on characterizing the behavioral response and the self-centering capacity of a hybrid NiTi SMA-steel-reinforced shear wall compared to a steel-reinforced wall. The original wall identifiers were SWS-R for the steel-reinforced wall and SWN for the hybrid NiTi SMA-reinforced wall. The first two letters "SW" represent the structural element type (shear wall), followed by "S" to denote the steel wall with local repairs "-R." The "N" identifier following "SW" represents the hybrid NiTi SMA-steel-reinforced wall. The base of the original steel wall, SWS-R, experienced honeycombing regions that were locally repaired with SCC. After testing the original walls by Morcos and Palermo,[10] both walls were repaired and renamed RSWS-R and RSWN to differentiate between the original and repaired walls.

Original walls

Wall details—The original walls were designed based on the seismic provisions for ductile walls prescribed by CAN/CSA A23.3-04,[10,18] respecting the reinforcement limits specified by the design standard. (Note that the original walls were similar to the walls reported by Abdulridha and Palermo,[9] which were designed and constructed based on the requirements for ductile walls in CAN/CSA A23.3-04, the design standard that was current at the time.) The design of the SMA wall was similar to the steel-reinforced wall as no code provisions exist for SMA-reinforced structural components. The walls had identical nominal dimensions, the major difference consisting of the longitudinal reinforcement in the boundary zones. The walls had a rectangular cross section, an aspect ratio (height-to-length ratio) of 2.2, and were 2200 mm in height, 1000 mm in length, and 150 mm in thickness. This aspect ratio was selected to promote flexural-dominant behavior. The walls were cast above foundation beams that were 1600 mm long, 500 mm high, and 1000 mm wide, which facilitated the anchorage of the walls to the strong floor of the laboratory. Additionally, loading beams 1600 mm long, 400 mm high, and 400 mm wide were monolithically cast with the walls to distribute the applied lateral loading.

Within the web region, the walls contained two layers of 10M bars (11.3 mm diameter, 100 mm^2 area) spaced at 150 mm in both the vertical and horizontal directions. The boundary zones were reinforced with four vertical bars confined by 10M closed stirrups spaced at 75 mm within the plastic hinge region and 150 mm above it. The vertical reinforcing bars in the boundary zones of SWS-R consisted of continuous 10M bars. The boundary zones of SWN contained 12.7 mm diameter smooth SMA bars in the plastic hinge region, connected through mechanical couplers with No. 13 (12.7 mm diameter, 129 mm^2 area) bars extending above the plastic hinge region. The reinforcement details of Wall SWN are shown in Fig. 1. The SMA bars extended 900 mm within the plastic hinge region and 300 mm into the foundation beam. A noninvasive method of mechanical coupling, based on forging the bar ends and using threaded couplers, was employed to connect the SMA bars to the deformed No. 13 reinforcement. Additional details on the design and fabrication of the original walls can be found elsewhere.[10,19]

Damage characteristics—The original walls were tested under reversed cyclic lateral loading following a protocol established by FEMA 461[20] and ATC-24,[21] which consisted of applying increasing lateral displacements until failure. Wall SWS-R sustained a peak load of 125 kN at 23 mm lateral displacement in the positive direction of loading, and SWN reached a peak load of 121 kN at 98 mm lateral displacement in the negative direction of loading.

For both walls, the first cracks propagated along the base at a lateral displacement of 1.2 mm. For SWS-R, subsequent

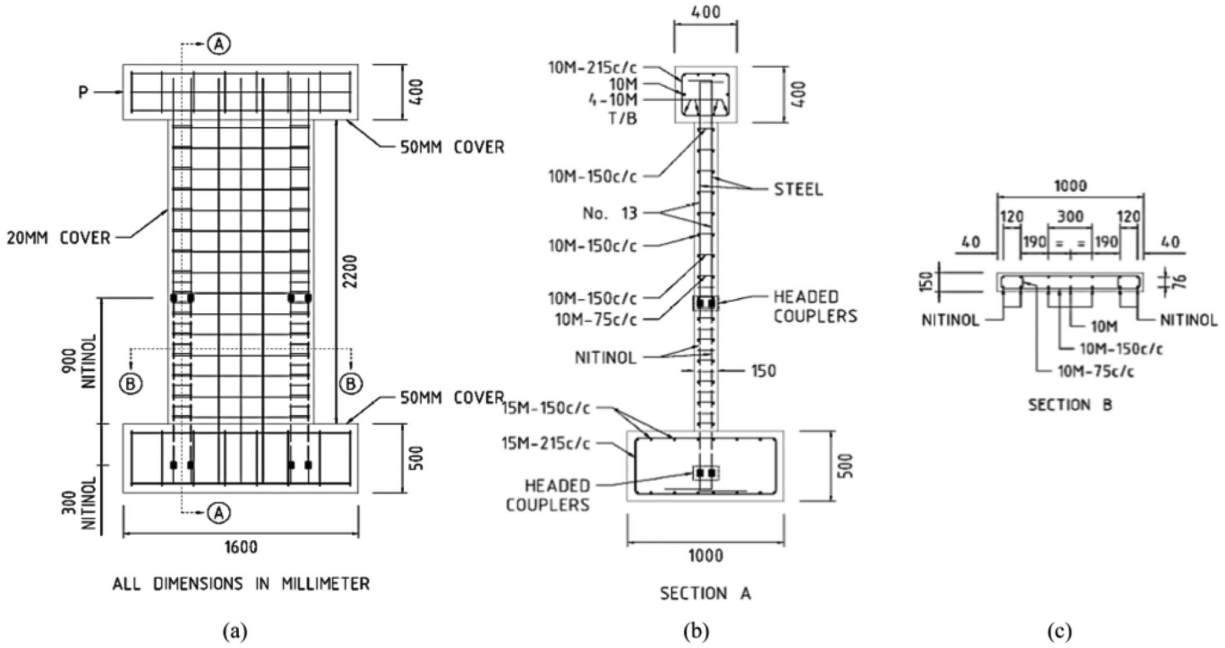

Fig. 1—Nominal dimensions and reinforcement details for Wall SWN: (a) elevation view; (b) section A-A; and (c) section B-B. (Taken from Morcos.[19])

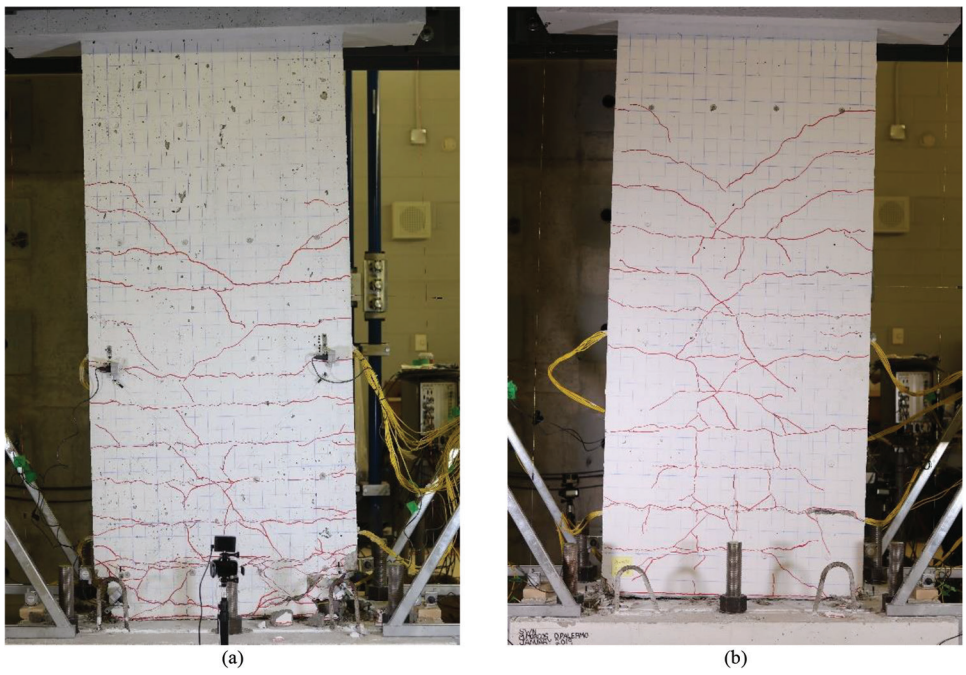

Fig. 2—Conditions of original walls after testing: (a) SWS-R; and (b) SWN. (Taken from Morcos.[19])

loading cycles led to the development of additional flexural cracks that propagated across the length of the wall and were spaced at approximately 150 mm over the height of the plastic hinge zone, as shown in Fig. 2(a). Additionally, flexural-shear cracks inclined at approximately 45 degrees developed. Crushing and spalling of concrete were pronounced around the toe regions of the wall. The loading cycles at an imposed lateral displacement of 72 mm led to the fracture of multiple vertical reinforcing bars in the boundary zones. Two bars fractured during the first positive excursion near the outer face, followed by the fracture of the two opposite bars during the negative excursion. The second positive cycle resulted in the fracture of the second row of reinforcing bars in the boundary zone, which concluded the test.

Wall SWN developed a crack pattern that was noticeably different compared to SWS-R, as shown in Fig. 2(b). One dissimilarity pertains to the propagation of flexural cracks, some of which did not extend over the entire length of the wall and remained confined to the web region. The spacing of the cracks within the web region was similar to that observed for SWS-R. Within the boundary zones, however, over the height of the plastic hinge region, the crack spacing was approximately twice the distance, approximately 300 mm. Additionally, three vertical cracks developed in the web, aligned with

Fig. 3—First stage of concrete removal and damage of reinforcing bars: (a) SWS-R; and (b) SWN.

the position of the vertical reinforcing bars. As the loading progressed, one flexural crack along the base and another at 300 mm above the base became dominant, developing significantly larger widths compared to the rest of the cracks. Flexural-shear cracks also developed, extending up to 1900 mm from the base, approximately 300 mm higher compared to Wall SWS-R. At a lateral displacement of 72 mm, rocking of the wall about the dominant flexural crack along the base was pronounced. Crushing of concrete in the toe regions was observed, albeit not as severe as SWS-R. The vertical bars in the web, closest to the boundary region, ruptured during the first negative excursion at 108 mm displacement. The web reinforcing bars placed along the centerline of the wall ruptured during the first imposed lateral displacement of 120 mm in the negative direction. The second positive excursion at 120 mm resulted in the rupture of the web reinforcement closest to the left boundary zone; this led to the termination of the test. No damage was observed in the SMA bars.

Both walls developed similar strength capacities; their overall responses, however, were marked by several significant differences. Compared to SWS-R, Wall SWN had a lower yield secant stiffness owing primarily to the lower stiffness of the SMA bars relative to the steel bars. Additionally, the smooth surface of the SMA bars led to the development of wider flexural cracks and larger crack spacing in Wall SWN in comparison with Wall SWS-R. The failure mechanism experienced by Wall SWN was characterized by a markedly reduced degree of damage in terms of sliding of the base, concrete crushing, and distribution of cracking. Furthermore, the SMA bars in Wall SWN suffered no damage, remaining functional, while the steel bars in the boundary zones of SWS-R buckled and fractured. Further details on the performance of the original set of walls are available elsewhere (Morcos and Palermo[10] and Morcos[19]).

Repair procedure

The repair procedure consisted of the construction of a bracing system for the walls to facilitate the safe and complete removal of damaged concrete from the plastic hinge region, replacement and addition of steel reinforcing bars, construction of formwork, and casting of the ECC mixture. Damage above the plastic hinge region, specifically concrete cracking, was not remediated in the repair strategy.

Concrete removal—Concrete removal was performed in three stages that allowed for a progressive investigation of the extent of the damage. The initial stage consisted of removing concrete over a height of 300 mm, as shown in Fig. 3, which revealed extensive damage experienced by the steel reinforcement in the form of buckling and fracture, and no observable damage for the SMA bars. The second stage involved removing concrete from the boundary regions over the entire plastic hinge length (900 mm in height from the base). No additional damage to the reinforcing bars was observed over this length for either of the walls. In addition, the coupling mechanism that connected the SMA bars to the No. 13 bars had no visible damage. During the third and final stage, the concrete was removed from the entire plastic hinge region and over a depth of approximately 60 mm into the foundation beam, as shown in Fig. 4. The concrete removal from the foundation was necessary to provide sufficient height to couple the remaining existing bars with the replacement segments, and for the repair ECC to penetrate the foundation to form a shear key.

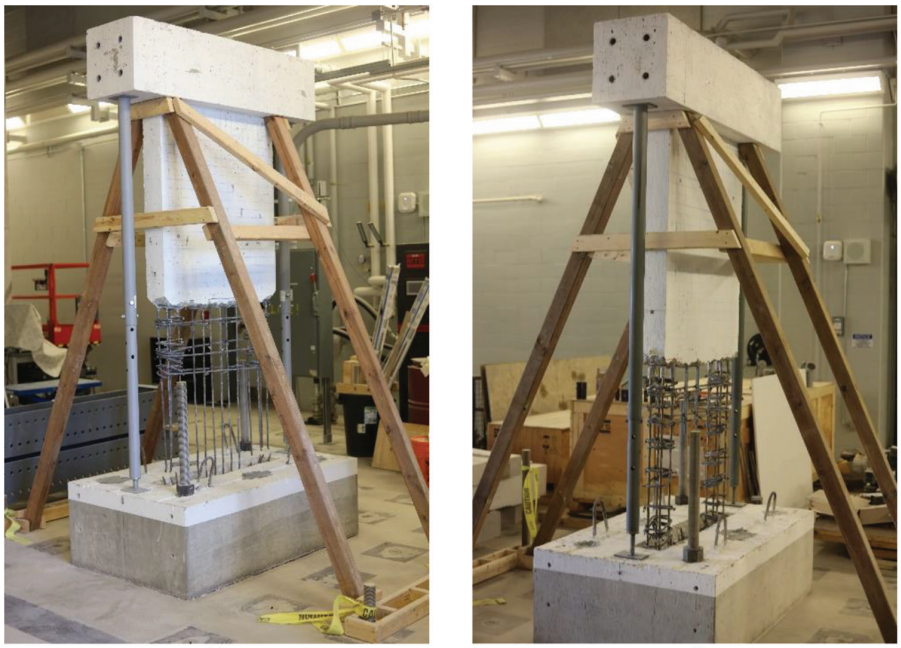

Fig. 4—Final stage of concrete removal: (a) SWS-R; and (b) SWN.

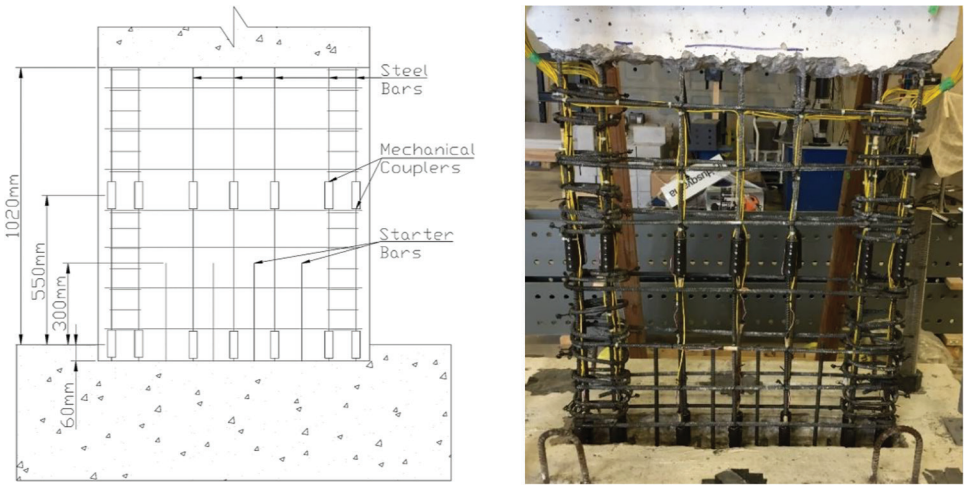

Fig. 5—Reinforcement layout of Wall RSWS-R in plastic hinge region.

The primary reasons for choosing this repair procedure were the extent of damage in the plastic hinge region and the opportunity to assess the behavior of the walls repaired with ECC in the plastic hinge region as part of a hybrid system. In addition, employing the same repair strategy for both walls permitted a direct comparison between their responses.

Replacement and addition of reinforcing bars—The damaged vertical steel reinforcing bars were removed and replaced with new segments of identical 10M bars. Shear-off mechanical couplers were used to connect the replacement segments to the remaining bars. In addition, four 10M starter bars, spaced at 150 mm along the base of the wall and extending 300 mm from the base, were provided in both walls to address the rocking and sliding observed at the base of the wall during testing of the original walls. Shown in Fig. 5 and 6 is the reinforcement layout within the repaired regions for RSWS-R and RSWN, respectively. For RSWS-R, all vertical bars were replaced, while for RSWN, only the vertical reinforcement in the web needed replacement as the SMA bars were undamaged. The ties in the boundary regions and the shear reinforcement of both walls were reused as no damage was observed.

First, the buckled and ruptured reinforcing bars were removed with an angle grinder, 500 mm from the base and slightly below the foundation level. The ends of the remaining reinforcing bars were then prepared with a belt sander to create a flat cross section to ensure a butt-end connection in the couplers with the replacement segments. Thereafter, the starter bars were installed. A rotary hammer was used to drill holes into the foundation, 12.5 mm in diameter and 125 mm in depth. The extent of drilling was based on the specifications required for the adhesive epoxy to ensure a proper bond. After the placement of the starter bars, the replacement segments of the vertical reinforcement were connected to the remaining bars using positional couplers. The couplers were 100 mm long and employed lock-shear

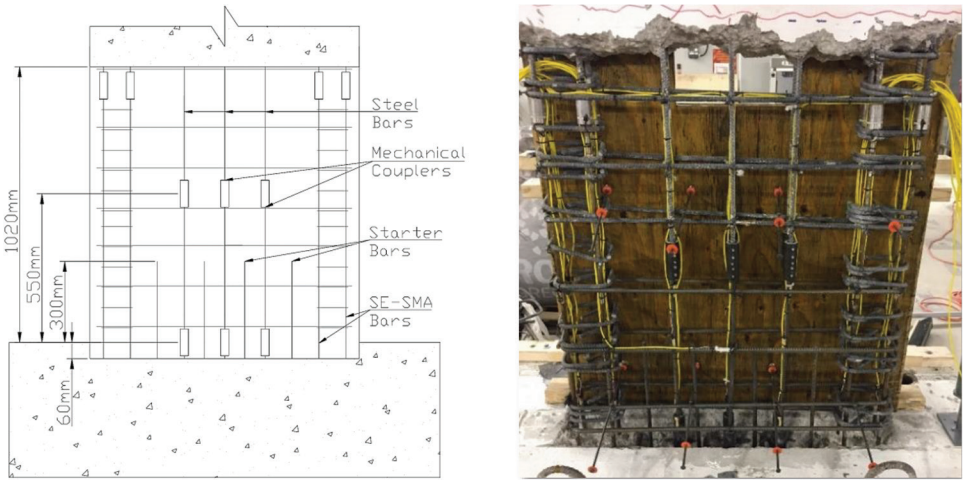

Fig. 6—Reinforcement layout of Wall RSWN in plastic hinge region.

Table 1—Mixture design proportions for 75 L batch

PVA fibers, kg									
ϕ = 0.10 mm	ϕ = 0.04 mm	Cement, kg	Fly ash, kg	Silica fume, kg	Slag, kg	Sand, kg	Water, kg	HRWRA, kg	Volume, L
0.94	0.94	30	50	8.25	3.38	33.38	23.33	0.75	75

bolts and serrated grip rails to mechanically splice the bars inserted from either end. An air impact wrench was used to tighten the bolts of the couplers.

Construction of formwork and casting of ECC—Plywood, 12.5 mm thick, was used as the main formwork component. Dimensional studs, 38 x 89 mm (2 x 4 in.), braced the plywood in the vertical and horizontal directions. In addition, snap ties were installed for additional resistance. A 200 x 300 mm opening was provided at the top of the formwork for concrete placement. The formwork design is illustrated in the Appendix, Fig. A.1.

The ECC was batched and mixed in-house, following a mixture design proposed by Eshghi,[22] with two modifications: the addition of smaller-diameter PVA fibers (ϕ = 0.04 mm) and the use of a different high-range water-reducing admixture (HRWRA) to obtain a flow between 200 and 250 mm, as per ASTM C1856/C1856M-17.[23] As such, two different types of PVA fibers were employed in this mixture, one with a 0.1 mm diameter and 1200 MPa tensile strength, and the other with a 0.04 mm diameter and 1560 MPa tensile strength. Both fiber types were 12 mm in length. Several trials were conducted to reach the final mixture design, summarized in Table 1. The objective was to achieve a mixture that provided post-cracking ductility,[24] while the compressive strength was not a controlling factor. The former was deemed critical for providing improved concrete damage control relative to the normal-strength concrete used in the original walls.

Casting deficiencies were encountered for Wall RSWS-R. The ECC was not adequately distributed along the top boundary of the plastic hinge, resulting in 50 mm gaps at both extremes of the wall, which gradually narrowed toward the center of the wall. To address this, SCC was cast in the affected areas. The curing procedure began immediately after formwork removal and was extended for 28 days. It consisted of covering the repaired regions of the walls with wet burlap sheets and a vapor barrier and watering every day until the end of the curing period. Figure 7 illustrates the repaired walls prior to testing.

Experimental setup and loading protocol

The experimental test setup is shown in Fig. A.2 in the Appendix and is the same as the setup used for the original walls, as designed by Morcos and Palermo.[10] Lateral loading was applied in a displacement-controlled mode through a single hydraulic actuator positioned along the centerline of the top beam of the walls. The actuator was attached to a steel bracket that was fixed to the strong wall. A lateral supporting frame was used to control out-of-plane displacements. It consisted of four vertical I-section steel columns bolted to the strong floor and connected to each other with four steel beams to provide a rigid restraining system, as shown in Fig. A.2. The lateral supporting frame was connected to the top beam of the walls through four casters placed on each lateral side of the steel beams.

The response of the walls was monitored and recorded with strain gauges, linear displacement transducers, and cable displacement potentiometers. The lateral and vertical displacements at different heights and the diagonal elongations in the plastic hinge zone of the repaired walls were measured. Additional details on the instrumentation are available elsewhere (Soto Rojas[24]).

The loading protocol for Walls RSWS-R and RSWN consisted of reverse cycles at multiples of the yield displacement (Δ_y) of Wall SWN to be consistent with the protocol applied to the original walls by Morcos and Palermo.[10] The approach was intended to evaluate the pre- and post-repair behavior of the walls under similar loading conditions. The yield displacement (Δ_y) of SWN was estimated from a preliminary pushover analysis to be 24 mm.[19] The loading cycles were divided into two groups: pre- and post-yield lateral displacement phases. The first loading phase

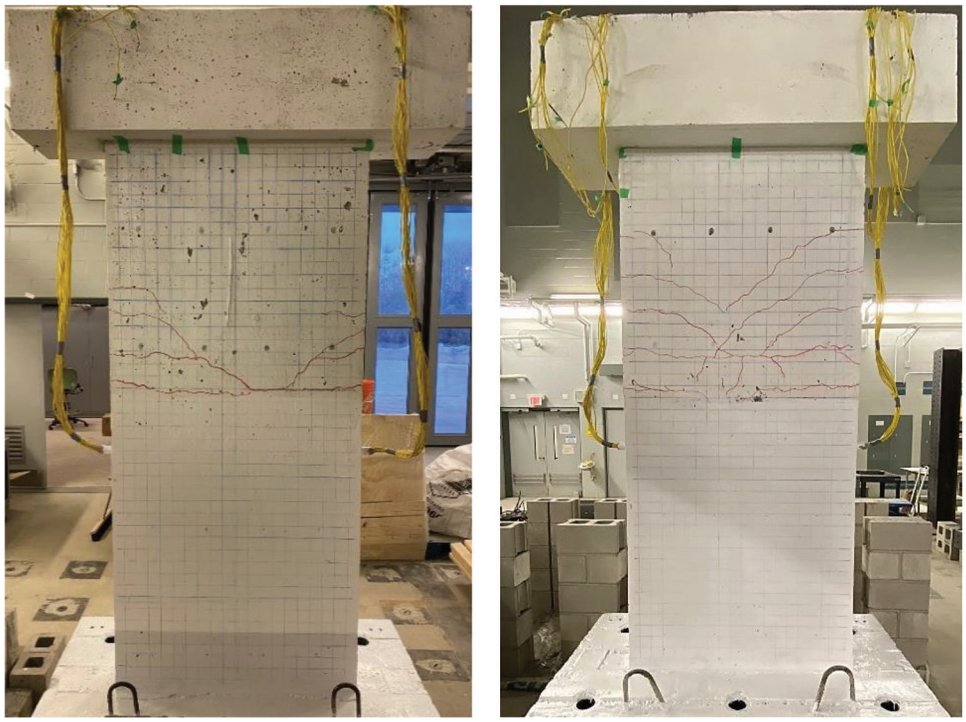

Fig. 7—Repaired walls prior to testing: (a) RSWS-R; and (b) RSWN.

consisted of three repetitions of seven targeted symmetrical displacements of $1/20\Delta_y$, $1/10\Delta_y$, $1/5\Delta_y$, $3/10\Delta_y$, $2/5\Delta_y$, and $1/2\Delta_y$ to reach the yield displacement Δ_y; thereafter, two repetitive cycles were imposed with displacement increments of $1/2\Delta_y$ until $5\Delta_y$ for Wall RSWS-R (following Wall SWS-R). Wall RSWN (following Wall SWN) continued with three repetitive cycles for each target displacement up to $2\Delta_y$ and two cycles per subsequent displacement level thereafter. (Note that based on preliminary numerical analysis, the yield displacement of SWS-R was approximated as one-half the yield displacement of SWN; therefore, the walls were subjected to three repetitions of loading up to two times their respective yield displacements.)

TEST RESULTS

Material properties

Concrete properties—The compressive strength of the ECC and SCC was evaluated from standard compression tests on 75 x 150 mm cylinders. The average compressive strength of three cylinders for the ECC was 64 MPa for RSWS-R and 63 MPa for RSWN on the day of testing the walls. The SCC in RSWS-R had an average compressive strength of 59 MPa.

Four-point bending tests were performed to characterize the flexural strength of the ECC on two prism specimens: Prism P1 with the dimensions of 75 x 75 x 250 mm, and Prism P2 with the dimensions of 75 x 75 x 500 mm. The prisms were cast from the ECC batch for Wall RSWS-R and were tested at the age of 28 days. The corresponding average 28-day compressive strength of three cylinders for the ECC was 49 MPa. Shown in Fig. 8 are the load-displacement responses, exhibiting a noticeable ductile behavior, characterized by a plateau stage at the initiation of cracking and prior to reaching the peak load. The descending branch of

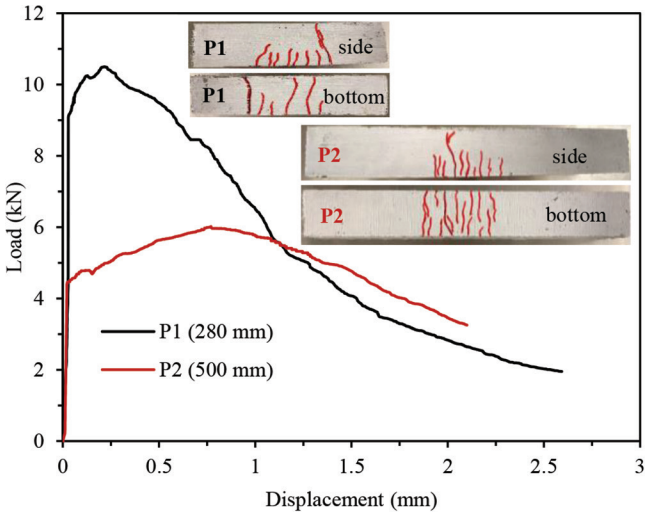

Fig. 8—Load versus midspan displacement of ECC flexural prisms and crack patterns at end of testing.

both prisms followed a gradual softening behavior. Additionally, both prisms developed a stiff initial response, where the first crack developed at 85% of the peak load for Prism P1 and 75% for Prism P2. The presence of the PVA fibers prevented a brittle failure mode; both prisms developed a localized dominant crack within the constant moment region and additional multiple finer cracks, as shown in Fig. 8. The fibers were able to bridge through and control the opening of the dominant crack, leading to the formation of other finer cracks. The maximum equivalent flexural strengths were 5.60 MPa for P1 and 6.42 MPa for P2; the corresponding midspan displacements were 0.22 mm for P1 and 0.77 mm for P2. (Note that the equivalent strengths were based on the gross section properties [Soto Rojas[24]]).

Table 2—Mechanical properties of reinforcing bars

Specimen ID	Bar	Yield strength, MPa	Modulus of elasticity, GPa	Tensile strength, MPa	Tensile strain, %	Rupture strain, %
SWS-R	10M*	428	197	558	14.7	17.4
SWN	10M*	435	186	564	14.0	15.8
SWN	No. 13*	463	203	627	12.3	16.5
SWN	SMA	338	42	1034	16.0†	16.0
RWS-R and RSWN	10M‡	430	175	537	16.4	26.2

*Mechanical properties following a repetition of the material tests. These updated properties differ from the values reported by Morcos,[19] Morcos and Palermo,[10] and Soto Rojas.[24]

†Strain at rupture.

‡Based on cyclic tensile test of one bar reported by Soto Rojas.[24]

Reinforcement properties—The mechanical properties of the 10M bars used in the repaired region of the walls were determined from standard coupon tests. Table 2 summarizes the properties of the reinforcing bars used in the original walls and the replacement bar segments used in the repair.

To assess the recovery capacity of the SMA bars, Morcos[19] performed a hybrid monotonic loading with a 6% strain cycle on an SMA bar used in Wall SWN. Shown in Fig. 9 is the comparison between the stress-strain response for the SMA bar and a 10M reinforcing bar used in the original walls. The superelasticity property of the SMA bar is evident; at a 6% strain, the SMA developed a stress of 495 MPa, and thereafter, when unloaded to zero stress, the SMA experienced a negligible plastic offset of 0.18% strain prior to reloading to failure. The SMA failed prematurely by rupture of the top conical head of the mechanical coupler used in the original SWN wall at a stress of 1034 MPa and a corresponding 16% strain.[19] At a 6% strain, the 10M steel bar was in the strain-hardening phase and at a stress level of 534 MPa. Unloading to zero stress, the steel bar experienced a residual strain of approximately 6%. Thereafter, the steel bar was loaded to failure, reaching a maximum tensile strength of 584 MPa at a corresponding strain of 16.6%.

Cracking characteristics

Figure 10 illustrates the cracking patterns after testing Walls RSWS-R and RSWN. The existing cracks from the initial testing are highlighted with red and the new cracks are marked with green. At 4.8 mm displacement (0.2% drift) Wall RSWN developed the first flexural crack in the repaired region, 425 mm above the base; the crack was 0.3 mm wide and 300 mm long. During the last repetition at 4.8 mm in the negative direction, a previously existing flexural crack located above the repaired region, 1250 mm from the base, widened and reached 0.25 mm in width. RSWS-R developed no cracks in the repaired region at this displacement level and the existing cracks did not experience growth.

Wall RSWS-R developed the first crack in the repaired region during the first cycle of 12 mm displacement (0.5% drift) in the negative direction; the crack was 250 mm long and surfaced 25 mm from the base of the wall. Another crack, 0.15 mm wide and 25 mm long, appeared during the second repetition in the positive direction at 250 mm from the base. In addition, two flexural-shear cracks, 0.15 mm in width, developed at 1550 and 1650 mm from the base of the wall.

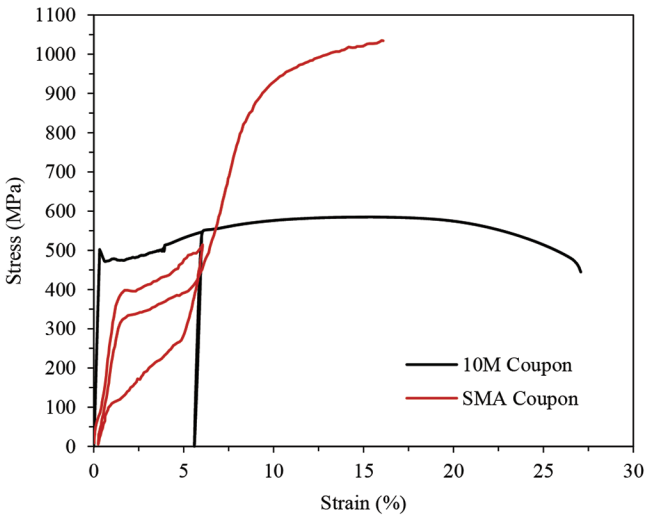

Fig. 9—Stress-strain response with 6% strain cycle of 10M steel and SMA bars. (Adapted from Morcos.[19])

Both walls developed major cracks at a displacement of 24 mm (1% drift). For Wall RSWS-R, a 3.0 mm wide flexural crack formed at 275 mm from the base. The negative excursions propagated this crack through the entire length of the wall. This localized damage was attributed to the change in the wall's stiffness at that location due to the presence of the starter bars and mechanical couplers. Additional shorter cracks developed on both sides of this major crack. Above the repaired region, three new 0.1 mm-wide shear cracks developed. Similarly, during the loading excursions at 24 mm lateral displacement, Wall RSWN developed a major 5.0 mm wide horizontal crack extending through the length of the wall, approximately 500 mm from the base. Two hairline shear cracks branched downward at a 45-degree angle from the major horizontal crack, and two existing hairline shear cracks located above the repaired region reopened and extended for an additional 5 mm.

As the displacement levels increased, the cracks for both walls experienced an increase in width, accompanied by visible pullout and rupture of the fibers. For Wall RSWS-R, the major horizontal crack extended along the entire length and through the thickness, dividing the wall into two sections that were mainly connected by the longitudinal steel reinforcement. During the loading cycles at 60 mm (2.5% drift), two longitudinal steel bars in the right boundary region of RSWS-R ruptured. At this displacement level, the cracks within the repaired region of the RSWN wall became wider

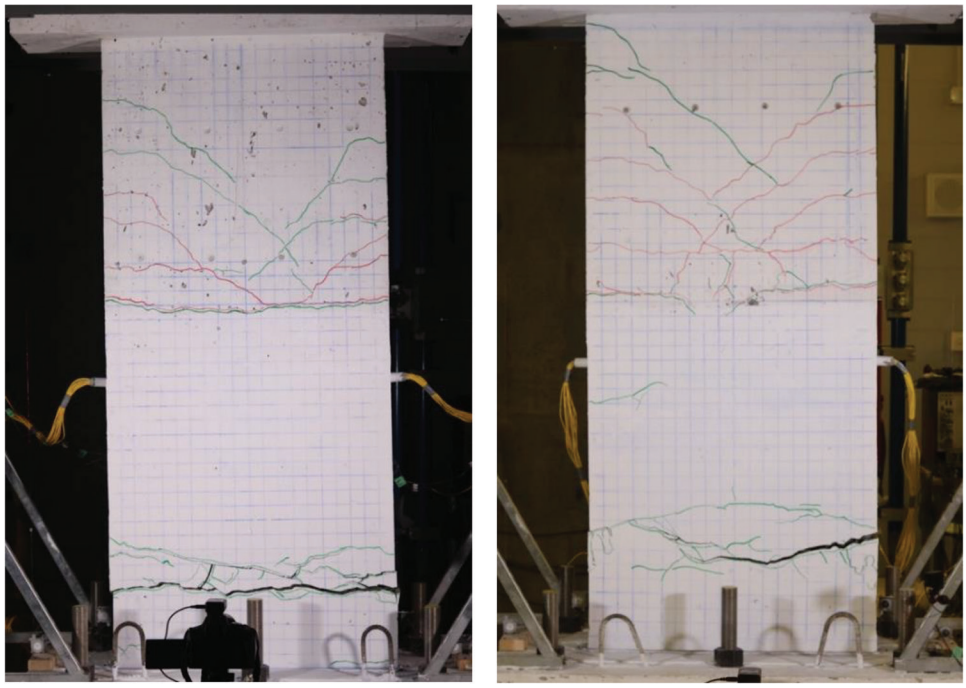

Fig. 10—Repaired walls after testing: (a) RSWS-R; and (b) RSWN.

without undergoing any propagation, with the major horizontal crack opening to 20 mm. Unlike the steel-reinforced wall, vertical cracks appeared on the right side of the wall and are attributed to debonding of the SMA bars. The same crack pattern was visible on the left side of the wall due to the loss of bond between the SMA bar and the surrounding concrete.

At the 72 mm displacement cycle (3% drift), testing of RSWS-R was terminated. The cracking characteristics did not change throughout this cycle, except for the dominant horizontal crack that extended to a width of 30 mm without recovery. Three longitudinal steel bars ruptured in the right boundary region by the end of the second repetition, while two bars ruptured in the left boundary region. At the end of testing, Wall RSWS-R experienced a lateral offset of approximately 20 mm along the dominant horizontal crack.

Testing of Wall RSWN proceeded with higher lateral displacements, up to 96 mm (4.0% drift). At 84 mm lateral displacement (3.5% drift), during the negative loading cycle, Wall RSWN experienced rupture of one longitudinal steel bar on the right side of the web region, adjacent to the SMA bars. The right side of the dominant horizontal crack widened to 31 mm. Testing was terminated at the end of the first cycle at 96 mm (4% drift). During loading to the positive direction, a longitudinal steel bar ruptured on the left side of the web region. Furthermore, in the final excursion in the negative direction, two longitudinal reinforcing bars located on the right side of the web region were ruptured.

Load-displacement response

The lateral load-displacement responses of the walls pre- and post-repair are illustrated in Fig. 11. The displacements were based on readings from the cable potentiometer installed at the midheight of the loading beam, which recorded measurements relative to the foundation. The performance of the repaired walls is marked by a higher lateral load resistance in comparison to the original walls and comparable displacement capacity. Wall RSWS-R dissipated more energy than Wall SWS-R, with slightly wider hysteretic curves characterized by the development of higher loads for the same displacements, as shown in Fig. 11(a). Similarly, a significant increase in the lateral strength was observed for Wall RSWN (Fig. 11(b)). Wall RSWN experienced a reduction in drift capacity relative to the original wall. No significant difference in pinching was observed in the repaired SMA wall in comparison to the original SMA wall.

Table 3 summarizes performance parameters for the original and repaired walls at the yield, peak, and ultimate points, calculated as an average from the positive and negative directions. Based on the reduced stiffness equivalent elastoplastic method,[25] the yield point was determined with a secant stiffness passing through the load-displacement response at 75% of the average nominal strength. The average yield load for Wall RSWS-R was 127 kN with a corresponding average yield displacement of 13.6 mm (0.6% drift). Wall RSWN had an average yield load of 123 kN and an average yield displacement of 30.9 mm (1.3% drift). Both walls had a nearly linear response prior to yielding, with Wall RSWN exhibiting a softer response due to the lower modulus of elasticity of the SMA bars compared to the steel reinforcement.

The post-yield behavior of Wall RSWS-R was marked by a steep development of load capacity prior to reaching the peak load. Conversely, Wall RSWN exhibited a sustained plateau with only a minor increase in load. In addition, the displacement recovery capacity of Wall RSWN was significantly more pronounced in comparison to RSWS-R; at the displacement level of 24 mm (1% drift), Wall RSWN experienced a residual displacement of 4.9 mm, while the residual displacement in Wall RSWS-R was 11 mm.

Table 3—Average performance points of original and repaired walls

Specimen ID	Yield			Peak			Ultimate		
	δ, mm	Drift, %	Load, kN	δ, mm	Drift, %	Load, kN	δ, mm	Drift, %	Load, kN
SWS-R	8.7	0.4	98	30.0	1.3	118	60	2.5	101
RSWS-R	13.6	0.6	127	29.3	1.2	145	56	2.3	128
SWN	45.0	1.9	93	91.0	3.8	118	103	4.3	113
RSWN	30.9	1.3	123	59.0	2.5	137	84	3.5	124

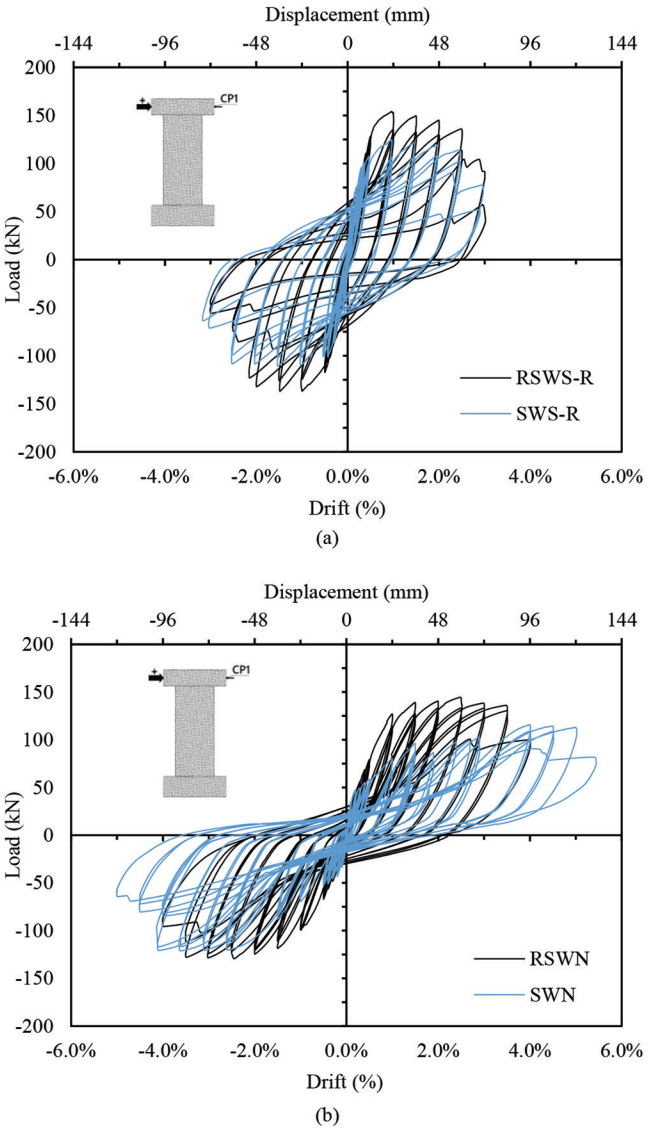

Fig. 11—Lateral load-displacement response of walls: (a) SWS-R and RSWS-R; and (b) SWN and RSWN.

Wall RSWS-R had an average peak lateral load capacity of 145 kN at an average displacement of 29 mm (1.2% drift). During loading to the positive direction at the first excursion of 24 mm (1% drift), RSWS-R developed a major crack located 300 mm above the base of the wall that corresponded to the peak load for the positive direction. The peak load in the negative direction occurred during the first repetition at 36 mm (1.5% drift) when a similar crack appeared on the opposite side. Wall RSWN had an average peak load of 137 kN with an average displacement of 59 mm (2.5% drift).

The post-peak response of both walls was dominated by the major cracks that developed above the starter bars. The ultimate point was established based on a 20% reduction in the lateral load capacity or the displacement cycle prior to the fracturing of the reinforcement. After the peak point, Wall RSWS-R experienced a gradual degradation of lateral load capacity, leading to an average ultimate load of 128 kN at an average displacement of 56 mm (2.3% drift), which represented the last cycle prior to rupturing of the longitudinal steel reinforcement in the boundary region. Wall RSWN sustained an average ultimate load of 124 kN with an average ultimate displacement of 84 mm (3.5%). The SMA bars located in the boundary region experienced no damage; however, the longitudinal steel reinforcing bars in the web region ruptured and marked the termination of the test.

DISCUSSION OF RESULTS

Envelope load-drift response

Figure 12 compares the lateral load-drift envelopes from the positive loading excursions of Walls SWS-R, RSWS-R, and RSWN and the negative loading excursion of Wall SWN. The negative loading envelope was chosen for Wall SWN to avoid discussing and comparing results obtained from the asymmetrical positive loading of this specimen. The envelopes were developed from the first repetition of each displacement level in the loading direction.

The original steel wall, SWS-R, exhibited a higher initial stiffness in comparison to the repaired companion wall RSWS-R; this difference is attributed to the existing damage above the plastic hinge region in RSWS-R. For the SMA-reinforced walls, the responses were relatively similar up to 48 kN lateral loading, after which they diverged significantly, with the repaired wall exhibiting markedly stiffer behavior. The initial stiffnesses, determined at 1.2 mm displacement (0.05% drift), were 32.4 and 24.4 kN/mm for Walls SWS-R and SWN, respectively. Walls RSWS-R and RSWN developed initial stiffnesses of 20.1 and 15.4 kN/mm, respectively.

It may be observed that the repaired steel wall experienced global yielding at a larger drift relative to the original wall. Conversely, the repaired SMA wall experienced a yield drift that was smaller than the original wall. However, the repaired walls exhibited a significant increase in the corresponding lateral strength at yielding. In the post-yielding regime, the repaired specimens, Walls RSWS-R and RSWN, sustained increased lateral loads in comparison with the original walls. The trend continued up to failure. It is noteworthy that, as shown in Fig. 12, the shapes of the envelopes are similar for RSWS-R and SWS-R. The envelope of RSWN exhibits a

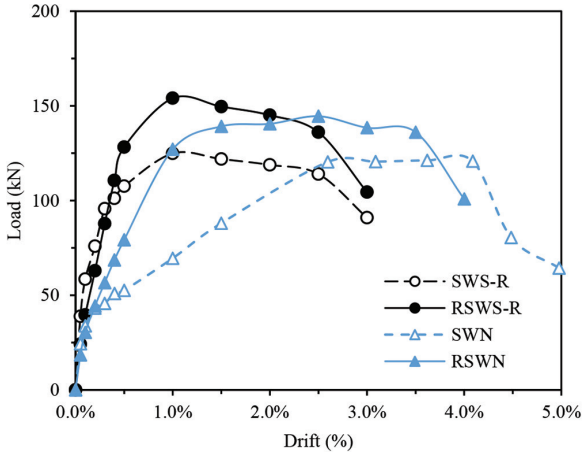

Fig. 12—Lateral load-drift envelopes of Walls SWS-R, RSWS-R, SWN, and RSWN.

response that can be satisfactorily characterized by bilinear behavior, whereas SWN provides a more pronounced trilinear response.

Cyclic rotation responses

The rotation responses were calculated from the vertical displacements recorded from the soffit of the top loading beam relative to the top of the foundation. The load-rotation behaviors are shown in Fig. 13. Overall, the SMA-reinforced walls exhibited larger rotations compared to the steel-reinforced walls. This behavior was observed for the original and repaired walls and is primarily attributed to the lower stiffness of the SMA bars and the development of dominant cracks. In addition, the SMA-reinforced walls were able to recover large rotations to a greater extent compared to the steel-reinforced walls due to the self-centering capacity of the SMA bars. The average rotation from the positive and negative loading cycles at yielding for Wall SWS-R was 5.5×10^{-3} rad, while the average rotation for SWN was 19.9×10^{-3} rad. The repaired Walls RSWS-R and RSWN exhibited 10.7×10^{-3} rad and 28.7×10^{-3} rad average rotations, respectively.

Wall RSWS-R sustained noticeably larger rotations compared to Wall SWS-R in the final loading cycles. This was due to the influence of ECC on the overall response, which led to the formation of a dominant crack in the repaired region and thus facilitated increased rotations. Repaired Wall RSWN also developed larger rotations compared to the original SWN wall, primarily due to the ECC material. At peak, Walls SWS-R and SWN developed average rotations of 12.3×10^{-3} rad and 36.7×10^{-3} rad, respectively. Repaired Walls RSWS-R and RSWN had average rotations of 20.1×10^{-3} rad and 45.6×10^{-3} rad, respectively. At ultimate, the original Wall SWS-R had a rotation of 21.7×10^{-3} rad, while SWN's rotation was 41.1×10^{-3} rad. The repaired Walls RSWS-R and RSWN at ultimate sustained 34.1×10^{-3} rad and 58.6×10^{-3} rad rotations, respectively.

Shear strain responses

The shear strains were calculated in the plastic hinge area following the approach suggested by Oesterle et al.[26]

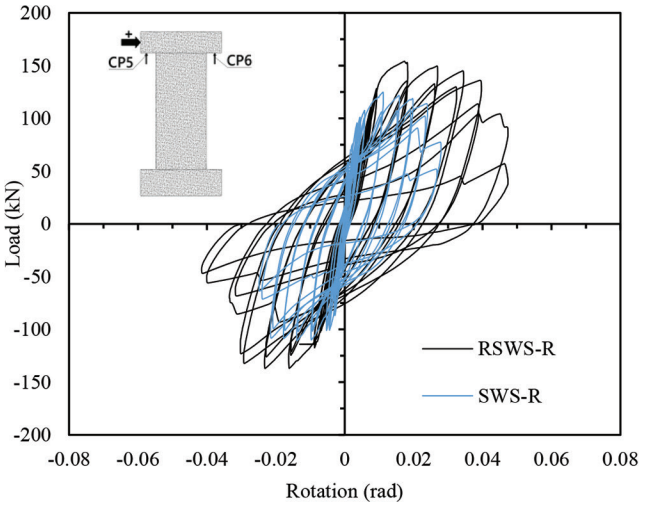

(a)

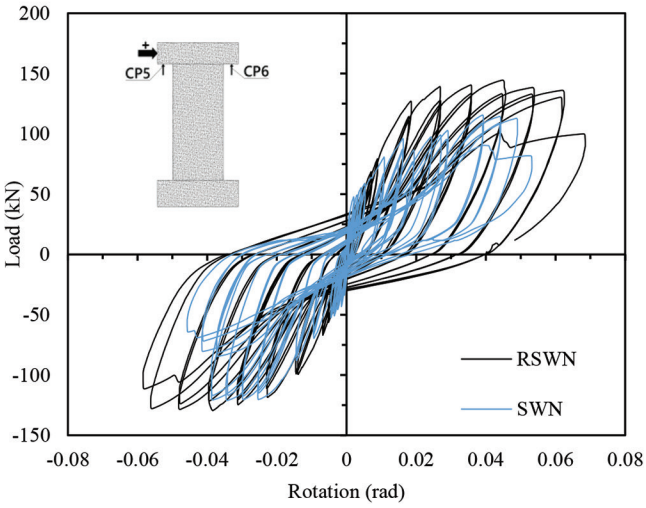

(b)

Fig. 13—Load-rotation responses of walls: (a) SWS-R and RSWS-R; and (b) SWN and RSWN.

$$\gamma = (\delta_1 d_1 - \delta_2 d_2)/2hl \quad (1)$$

where γ is the shear strain; d_1 and d_2 are the reference lengths of the cable potentiometers installed diagonally in the plastic hinge; δ_1 and δ_2 are the change in length of the diagonal cable potentiometers; and h and l are the vertical and horizontal projections of the cable potentiometers. The dimensions were the same for all walls, d_1 and d_2 were 1130 mm, and h and l were 800 mm. Figure 14 depicts the load-shear strain responses.

At yielding, the repaired walls experienced average shear strains of 1.5×10^{-3} rad for Wall RSWS-R and 4.4×10^{-3} rad for Wall RSWN. The original walls, SWS-R and SWN, developed at yielding average shear strains of 0.5×10^{-3} and 2.4×10^{-3} rad, respectively. At peak lateral load, Wall RSWN developed average shear strains of 6.75×10^{-3} rad compared to 4.0×10^{-3} rad for Wall RSWS-R. The original Walls SWN and SWS-R exhibited average shear strains at peak loads of 4.50×10^{-3} and 2.9×10^{-3} rad, respectively. As the lateral displacements increased, Wall RSWS-R experienced larger

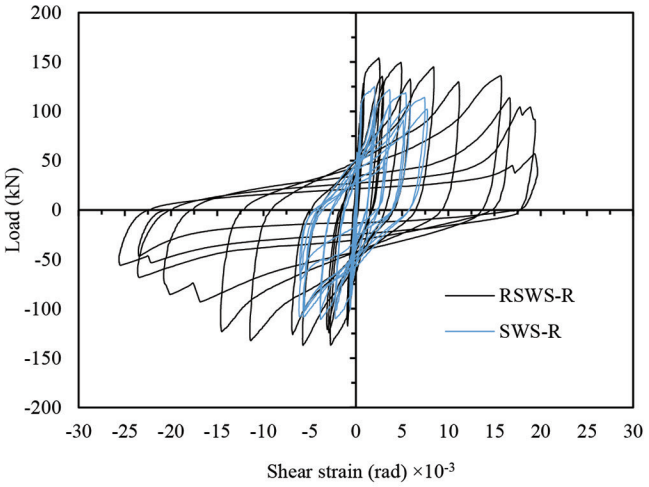

(a)

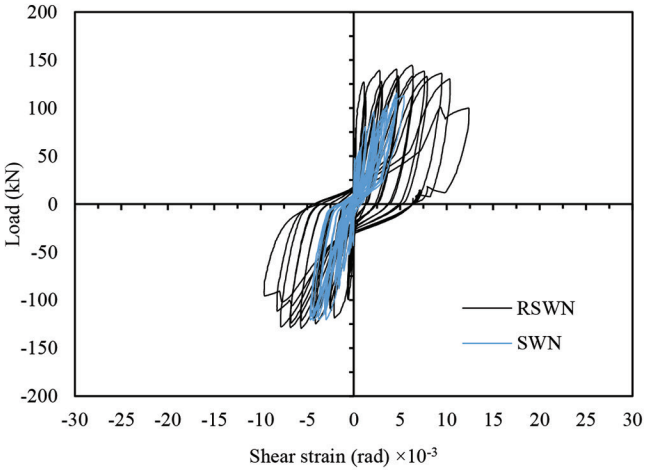

(b)

Fig. 14—Load-shear strain responses of walls: (a) SWS-R and RSWS-R; and (b) SWN and RSWN.

shear strains compared to Wall RSWN, reaching an ultimate average shear strain of 14.9 × 10^{-3} rad, while Wall RSWN was subjected to 9.1 × 10^{-3} rad. The ultimate average shear strains for SWS-R and SWN were 6.8 × 10^{-3} rad for Wall SWS-R and 4.6 × 10^{-3} rad for Wall SWN.

The repaired walls did not experience shear failure or significant shear damage, indicating that the shear capacity of ECC combined with the transverse reinforcement was not exceeded. The main difference between the repaired walls is denoted by the higher shear strain recovery capacity of the SMA wall, whereas the steel-reinforced wall sustained high residual shear strain. The recentering characteristics of the SMA bars promoted the symmetrical behavior of Wall RSWN, while the conventional steel wall experienced an asymmetrical response (ratcheting in one direction); similar responses were observed for the original walls. In addition, no accentuated pinching was observed in the walls, explained by the lack of shear cracks within the plastic hinge region. In comparison with the original walls, the repaired walls developed considerably larger shear distortions over the plastic hinge region, attributed mainly to the behavior of ECC and to the contribution of the starter bars. (Recall that the original walls experienced rocking at the base of the walls, which was controlled in the repaired walls.)

Energy dissipation

Figure 15 provides the load-displacement response of all walls at 36 mm (1.5% drift). The characteristics of the responses between each set of walls are similar, with the exception of higher loads measured for the repaired walls. The dissipated energy was calculated as the area encompassed by the loop of the first repetition of loading. At this displacement level, the energy dissipated by Wall RSWS-R was 6240 N·m, which represented 8% more energy than SWS-R, with a dissipated energy of 5765 N·m. Similarly, Wall RSWN dissipated 2700 N·m, a 22% increase over Wall SWN, with 2130 N·m of energy dissipated. The ECC used for the repaired walls contributed to a strength enhancement in the walls, leading to higher dissipated energy throughout testing. In addition, the starter bars shifted the critical section above the base of the wall, effectively reducing the lever arm and resulting in increased strength.

Figure 16 illustrates the energy dissipated at each drift level for the original and repaired walls. Up to a 0.5% drift, the energy dissipation for all the walls was comparable. Thereafter, it is evident that the repaired steel-reinforced wall dissipated more energy compared to the original wall. For the SMA walls, the difference in energy dissipation became more pronounced in the final loading cycles, with the repaired wall dissipating significantly more energy.

Recovery capacity

Figure 17 presents the recovery capacity-drift response of all the walls. The recovery capacity is calculated as the ratio of the difference between the peak displacement and the residual displacement to the peak displacement for each drift level. For Wall SWN, the negative loading direction was also included, due to a significant difference in response compared to the positive direction. For the remainder of the walls, the recovery capacity was similar for the positive and negative loading directions; as such, only the positive results are reported. The enhanced recovery attained by the repaired walls in the initial phase of testing was partly due to the preferred behavior of the ECC. In addition, the placement of the starter bars shifted the critical section away from the base of the wall, allowing for the characteristics of the ECC and SMA materials to better contribute to the response of the walls.

At the onset of testing, up to a 0.3% drift, the original and repaired steel-reinforced walls behaved in a similar manner. At a 0.4% drift, Wall SWS-R recovered 76% from the imposed displacement, while Wall RSWS-R recovered 85.4%. Similar behavior was experienced throughout testing; at a 1% drift, Wall SWS-R recovered 40.2%, whereas Wall RSWS-R recuperated 51.6%. At a 2% drift, Wall SWS-R recovered 29%, while Wall RSWS-R was able to retrieve 37.6%. The difference of approximately 10% in recovery capacities decreased as the walls approached failure.

The repaired SMA wall, RSWN, exhibited an improved recovery capacity up to a 1.5% drift, compared to both the

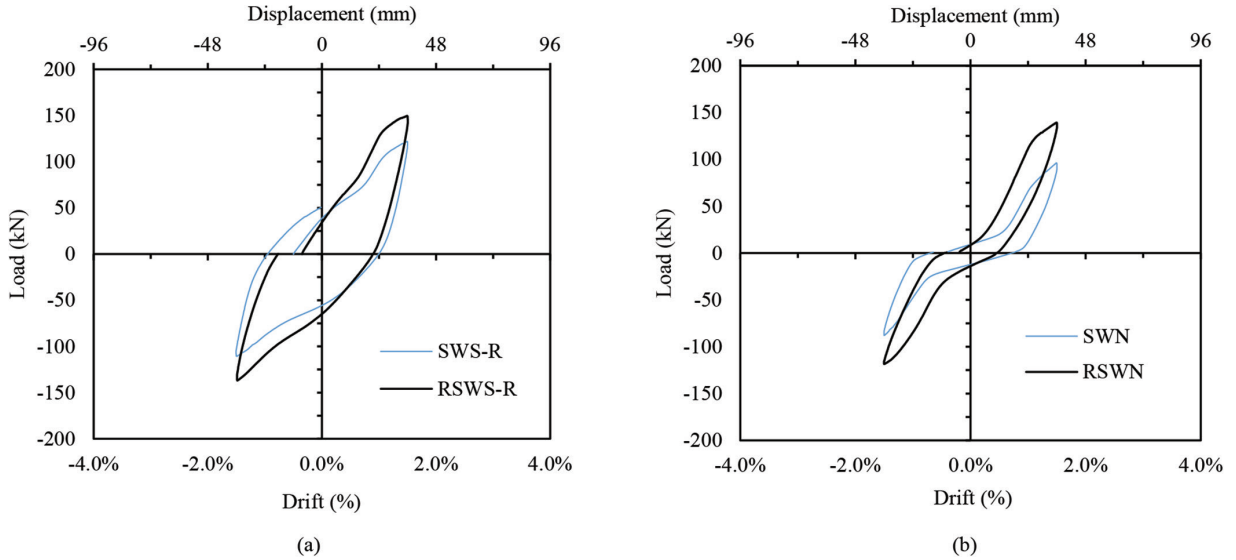

Fig. 15—Hysteretic response at 36 mm displacement (1.5% drift) of walls: (a) SWS-R and RSWS-R; and (b) SWN and RSWN.

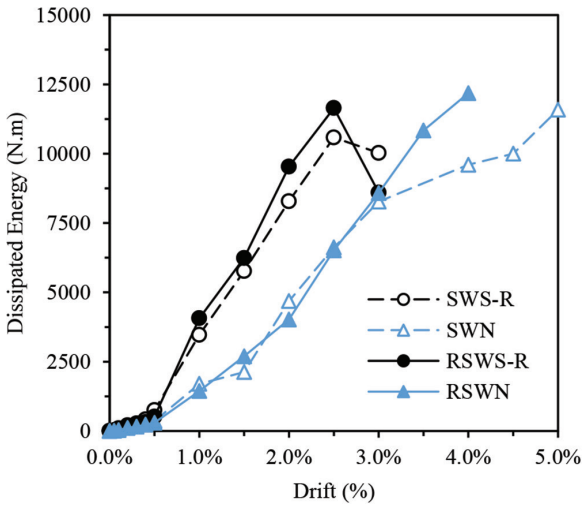

Fig. 16—Energy dissipated at different drift levels.

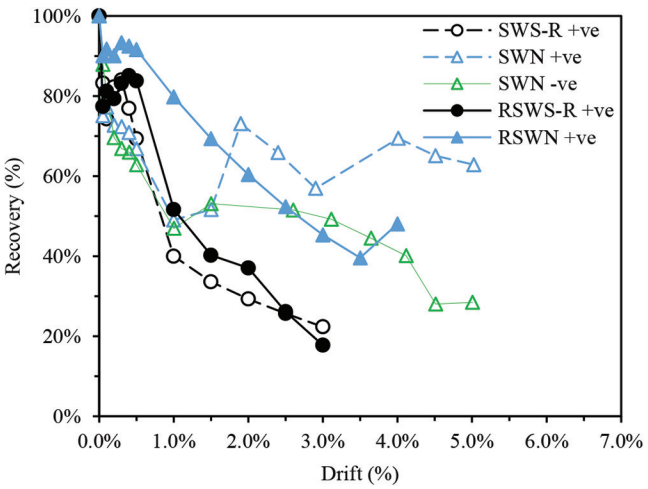

Fig. 17—Displacement recovery capacity-drift responses of walls: SWS-R and RSWS-R; and SWN and RSWN.

positive and negative responses of the original SWN wall. Thereafter, Wall SWN provided an enhanced recovery capacity in the positive loading direction compared to the repaired wall, which was maintained until failure. Compared to the recovery capacity of Wall SWN measured in the negative direction, the repaired wall exhibited a preferred response; the difference in recovery, however, was diminished as the walls approached failure, similar to the trend observed for the steel-reinforced walls. The primary reason behind the dissimilarity between the positive and negative loading responses for Wall SWN is attributed to the pronounced sliding at the base and rocking of the wall. Note that the increase of recovery for Wall RSWN at a 4% drift was the result of the fracturing of the longitudinal web bars, reducing the resistance to recovery.

Effect of starter bars

The addition of the starter bars in the web region of the repaired walls aimed to control the sliding of the walls along the cold joint between the ECC repair concrete and the existing concrete at the foundation level. In addition, the starter bars were used to prevent the rocking of the walls experienced by the original walls along their base. Controlling sliding and rocking resulted in a response that was controlled within the wall panel. This, in turn, ensured that the benefits of the ECC were realized. A cable potentiometer was installed 50 mm above the base of the walls to monitor the horizontal displacements throughout testing. The maximum lateral displacement was 0.38 mm for Wall RSWN and 0.31 mm for Wall RSWS-R. The negligible displacements validated that the addition of the starter bars eliminated sliding along the base of the walls. Furthermore, the starter bars eliminated the damage experienced by the original walls at the base. Figure 18 illustrates the state of the base of Walls SWN and RSWN at the end of testing. No significant cracking surfaced in the repaired walls along the height of the starter bars (300 mm) due to the high concentration of steel in this region, which created a rigid section, shifting the failure mode higher into the wall.

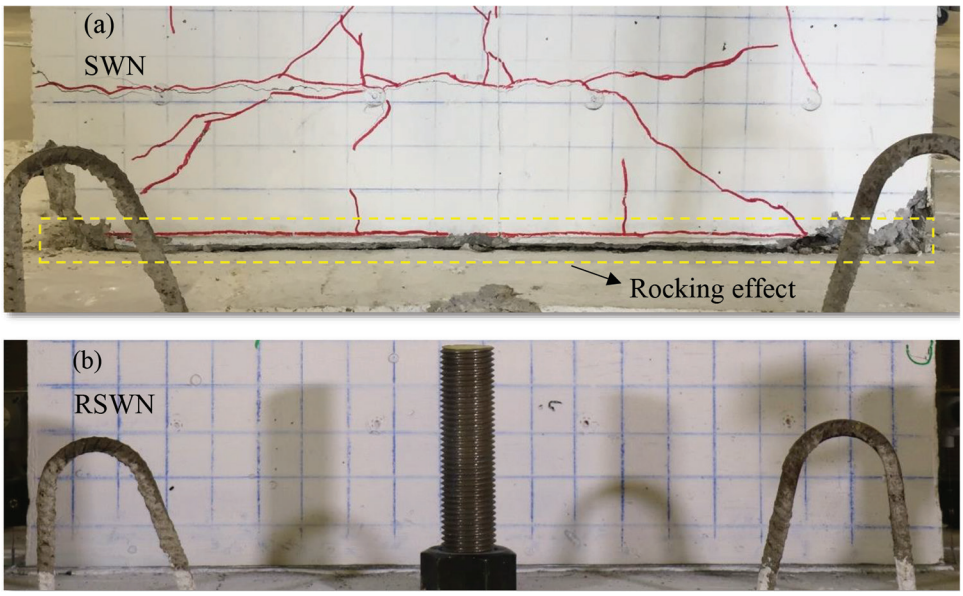

Fig. 18—State of base of walls at end of testing: (a) SWN; and (b) RSWN.

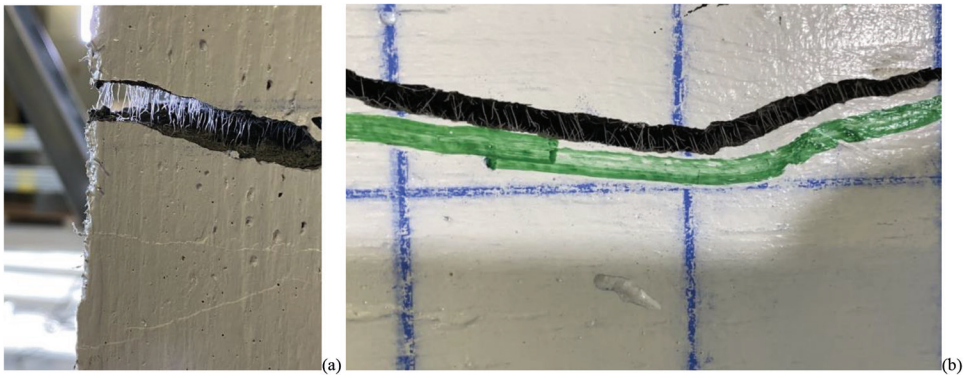

Fig. 19—Wall RSWN: Pulling out and fracturing of PVA fibers at localized cracks: (a) boundary zone; and (b) web region.

Failure modes

Figures 2 and 10 depict the crack patterns of the original and repaired walls at the end of testing. The influence of the ECC mixture is evident when comparing the state of the walls at failure. For the repaired wall, widespread cracking did not surface as was observed in the original walls (Fig. 2), and the formation of a more localized damage zone was evident (Fig. 10).

Replacing the conventional concrete with the ECC in the plastic hinge resulted in a delay in the damage experienced by the repaired walls at larger drifts. Moderate damage was detected up to a 1.5% drift for both repaired walls compared to a 0.5% drift for Wall SWS-R and a 0.3% drift for Wall SWN. This was associated with the effectiveness of the fibers in bridging the cracks at large displacements. The damage retention and crack recovery were sustained up to drifts of 2% for Wall RSWS-R and 2.5% for Wall RSWN. Thereafter, the fibers began pulling out from and fracturing at the localized major crack. The PVA fibers pulled out once the crack width exceeded the anchorage length of the fibers, approximately 6 mm. The major crack that formed in Wall RSWN at a height of 400 mm from the base illustrated the benefits of the fibers, which prevented the crack from widening up to drifts of 2.5%. Figure 19 is a close-up view of the PVA fibers pulling out and fracturing at the localized cracks located in the boundaries and web region of Wall RSWN. Note that similar behaviors were observed in both repaired walls.

CONCLUSIONS

Two previously tested shear walls were repaired and tested under reversed cyclic loading. One of the walls was reinforced with nickel-titanium (NiTi) superelastic bars in the boundary regions of the plastic hinge area, while the other wall contained steel reinforcement only. The repair involved the removal of heavily damaged concrete in the plastic hinge area, the replacement of ruptured and buckled steel reinforcement, the addition of starter bars, and the casting of engineered cementitious composite (ECC) to replace the concrete that was removed. The following conclusions are drawn from the experimental testing:

1. The repaired walls developed localized damage primarily within one-third of the plastic hinge region, as opposed to the original walls, which presented widespread cracking. The major benefit of localized damage relates to a potentially more accelerated repair process.

2. The lateral strength of the repaired walls was considerably higher compared to the original walls. The enhanced properties of the ECC were one of the main factors

contributing to the increase in capacity. Repaired Wall RSWS-R developed a peak lateral strength 23% larger compared to the original Wall SWS-R; both walls reached their peak strength at 30 mm lateral displacement. Wall RSWN had a 16% increase in peak lateral strength compared to SWN; the repaired wall developed its peak load at 66 mm lateral displacement, in comparison to 91 mm for SWN. The strength enhancement of the repaired walls led to generally higher dissipated energy.

3. The ultimate drift capacity of the repaired RSWS-R wall was marginally lower, 2.3% compared to 2.5% for SWS-R. A more pronounced reduction in ultimate drift was measured for Wall RSWN (3.5%) compared to SWN (4.3%).

4. Generally, enhanced recovery capacity was observed for the repaired walls compared to the original walls, primarily due to the enhanced behavior of ECC and the placement of the starter bars. (Note that this is true for the repaired shape memory alloy [SMA] wall relative to the negative direction of loading of the original wall.) The starter bars shifted the critical section away from the base of the wall, thus allowing for the ECC and SMA materials to better contribute to the response of the walls.

5. For both sets of walls, the SMA-reinforced walls exhibited larger rotations compared to the steel-reinforced walls on account of the lower stiffness of the SMA bars.

6. The repaired walls did not exhibit significant shear damage. Wall RSWN developed a higher shear strain recovery capacity compared to Wall RSWS-R, which sustained high residual shear strain. The recentering characteristics of the SMA bars promoted the symmetrical behavior of Wall RSWN, while the conventional steel wall experienced an asymmetrical response; similar responses were observed for the original walls.

In summary, the study presented herein demonstrates that NiTi SMA bars and ECC constitute a viable system for slender concrete shear walls. In general, the repair strategy enhanced the recovery and energy dissipation capacities, resulted in damage localization, and permitted the walls to exhibit enhanced shear distortion and rotation responses.

AUTHOR BIOS

Michael A. Soto-Rojas *is a Structural Engineer in Training with the Department of Highways and Public Works, Whitehorse, YT, Canada. He received his MASc from York University, Toronto, ON, Canada, in 2020. His research interests include engineered cementitious composites, shape memory alloys, and testing of concrete shear walls.*

Anca C. Ferche *is an Assistant Professor in the Department of Civil, Architectural and Environmental Engineering at The University of Texas at Austin, Austin, TX. She received her PhD from the University of Toronto, Toronto, ON, Canada, in 2020. Her research interests include performance assessment and analysis of reinforced concrete structures, concrete deterioration mechanisms, and rehabilitation of structures.*

Dan Palermo *is a Professor in the Department of Civil Engineering at York University. His research interests include seismic repair and retrofitting of concrete structures, nonlinear finite element modeling, seismic applications of shape memory alloys, ultra-high-performance steel fiber-reinforced concrete and engineered cementitious composites, tall masonry wall systems, and the response of structures to tsunami loading.*

ACKNOWLEDGMENTS

The authors acknowledge the funding provided by the Natural Sciences and Engineering Research Council of Canada (NSERC) through the Discovery Grants program (Grant: RGPIN-2017-05679).

REFERENCES

1. EN 1998-1:2004, "Eurocode 8: Design of Structures for Earthquake Resistance—Part 1: General Rules, Seismic Actions and Rules for Buildings," European Committee for Standardization, Brussels, Belgium, 2004, 231 pp.

2. FEMA P-1050, "NEHRP Recommended Seismic Provisions for New Buildings and Other Structures," Building Seismic Safety Council, Washington, DC, 2015.

3. Joint ACI-ASCE Committee 441, "High-Strength Concrete Columns: State of the Art (ACI 441R-96)," American Concrete Institute, Farmington Hills, MI, 1996, 13 pp.

4. ACI Committee 318, "Building Code Requirements for Structural Concrete (ACI 318-19) and Commentary (ACI 318R-19) (Reapproved 2022)," American Concrete Institute, Farmington Hills, MI, 2019, 624 pp.

5. Wallace, J. W.; Massone, L. M.; Bonelli, P.; Dragovich, J.; Lagos, R.; Lüders, C.; and Moehle, J., "Damage and Implications for Seismic Design of RC Structural Wall Buildings," *Earthquake Spectra*, V. 28, No. 1_suppl1, June 2012, pp. 281-299. doi: 10.1193/1.4000047

6. Elwood, K. J., "Performance of Concrete Buildings in the 22 February 2011 Christchurch Earthquake and Implications for Canadian Codes," *Canadian Journal of Civil Engineering*, V. 40, No. 8, Aug. 2013, pp. 759-776. doi: 10.1139/cjce-2011-0564

7. Pan, Z.; Wu, C.; Liu, J.; Wang, W.; and Liu, J., "Study on Mechanical Properties of Cost-Effective Polyvinyl Alcohol Engineered Cementitious Composites (PVA-ECC)," *Construction and Building Materials*, V. 78, Mar. 2015, pp. 397-404. doi: 10.1016/j.conbuildmat.2014.12.071

8. Mohammed, B. S.; Nuruddin, M. F.; Aswin, M.; Mahamood, N.; and Al-Mattarneh, H., "Structural Behavior of Reinforced Self-Compacted Engineered Cementitious Composite Beams," *Advances in Materials Science and Engineering*, V. 2016, 2016, Article No. 5615124, 12 pp. doi: 10.1155/2016/5615124

9. Abdulridha, A., and Palermo, D., "Behaviour and Modelling of Hybrid SMA-Steel Reinforced Concrete Slender Shear Wall," *Engineering Structures*, V. 147, Sept. 2017, pp. 77-89. doi: 10.1016/j.engstruct.2017.04.058

10. Morcos, M., and Palermo, D., "SMA-Reinforced Concrete Shear Walls Subjected to Reverse Cyclic Loading," *Proceedings of the Fifth International Conference on Smart Monitoring, Assessment and Rehabilitation of Civil Structures (SMAR 2019)*, Aug. 2019, Potsdam, Germany, 2019, 8 pp.

11. Morcos, M., and Palermo, D., "Numerical Modelling of Slender Superelastic-Shape Memory Alloy Reinforced Concrete Shear Walls," *Proceedings of 6th International Structural Specialty Conference (CSCE 2018)*, K. Arjomandi and A. El Damatty, eds., Fredericton, NB, Canada, June 2018, pp. 528-538.

12. Cortés-Puentes, L.; Zaidi, M.; Palermo, D.; and Dragomirescu, E., "Cyclic Loading Testing of Repaired SMA and Steel Reinforced Concrete Shear Walls," *Engineering Structures*, V. 168, Aug. 2018, pp. 128-141. doi: 10.1016/j.engstruct.2018.04.044

13. Saiidi, M. S.; O'Brien, M.; and Sadrossadat-Zadeh, M., "Cyclic Response of Concrete Bridge Columns Using Superelastic Nitinol and Bendable Concrete," *ACI Structural Journal*, V. 106, No. 1, Jan.-Feb. 2009, pp. 69-77.

14. Abdulridha, A.; Palermo, D.; Foo, S.; and Vecchio, F. J., "Behavior and Modeling of Superelastic Shape Memory Alloy Reinforced Concrete Beams," *Engineering Structures*, V. 49, Apr. 2013, pp. 893-904. doi: 10.1016/j.engstruct.2012.12.041

15. Saiidi, M. S., and Wang, H., "Exploratory Study of Seismic Response of Concrete Columns with Shape Memory Alloys Reinforcement," *ACI Structural Journal*, V. 103, No. 3, May-June 2006, pp. 436-443.

16. Youssef, M. A.; Alam, M. S.; and Nehdi, M., "Experimental Investigation on the Seismic Behavior of Beam-Column Joints Reinforced with Superelastic Shape Memory Alloys," *Journal of Earthquake Engineering*, V. 12, No. 7, 2008, pp. 1205-1222. doi: 10.1080/13632460802003082

17. Nehdi, M.; Alam, M. S.; and Youssef, M. A., "Seismic Behaviour of Repaired Superelastic Shape Memory Alloy Reinforced Concrete Beam-Column Joint," *Smart Structures and Systems*, V. 7, No. 5, 2011, pp. 329-348. doi: 10.12989/sss.2011.7.5.329

18. CAN/CSA A23.3-04 (R2010), "Design of Concrete Structures," CSA Group, Toronto, ON, Canada, 2004, 352 pp.

19. Morcos, M., "Seismic Behaviour of SMA-Reinforced Slender Concrete Shear Walls," master's thesis, York University, Toronto, ON, Canada, 2021, 446 pp.

20. FEMA 461, "Interim Testing Protocols for Determining the Seismic Performance Characteristics of Structural and Nonstructural Components," Applied Technology Council, Redwood City, CA, 2007, 138 pp.

21. ATC-24, "Guidelines for Cyclic Seismic Testing of Components of Steel Structures," Applied Technology Council, Redwood City, CA, 1992, 58 pp.

22. Eshghi, N., "Behaviour and Analysis of Strain Hardening Fiber Reinforced Cementitious Composites Under Shear and Flexure," MASc thesis, York University, Toronto, ON, Canada, 2018, 209 pp.
23. ASTM C1856/C1856M-17, "Standard Practice for Fabricating and Testing Specimens of Ultra-High Performance Concrete," ASTM International, West Conshohocken, PA, 2017, 4 pp.
24. Soto Rojas, M. A., "Behavior of Engineered Cementitious Composite-Repaired Superelastic-Shape Memory Alloy Reinforced Shear Walls," MASc thesis, York University, Toronto, ON, Canada, 2020, 289 pp.
25. Park, R., "State-of-the-Art Report: Ductility Evaluation from Laboratory and Analytical Testing," *Proceedings of the Ninth World Conference on Earthquake Engineering*, Tokyo-Kyoto, Japan, Aug. 1988, 12 pp.
26. Oesterle, R. G.; Fiorato, A. E.; Johal, L. S.; Carpenter, J. E.; Russell, H. G.; and Corley, W. G., "Earthquake Resistant Structural Walls - Tests of Isolated Walls," Portland Cement Association, Skokie, IL, 1976, 328 pp.

APPENDIX

The Appendix contains additional material supporting the discussion contained in the preceding journal paper.

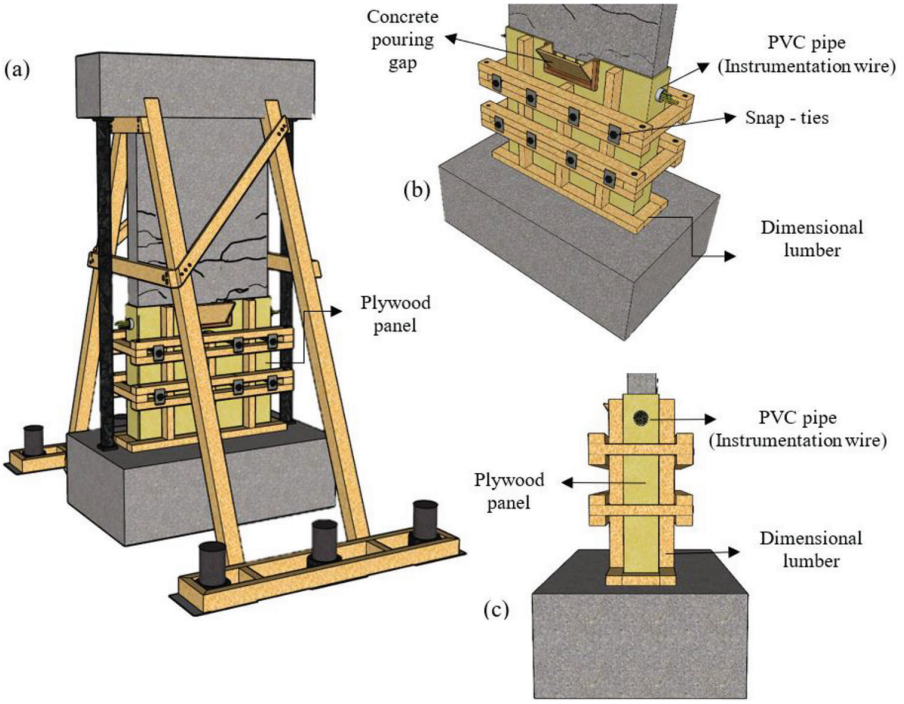

Fig. A1—Formwork design for plastic hinge.

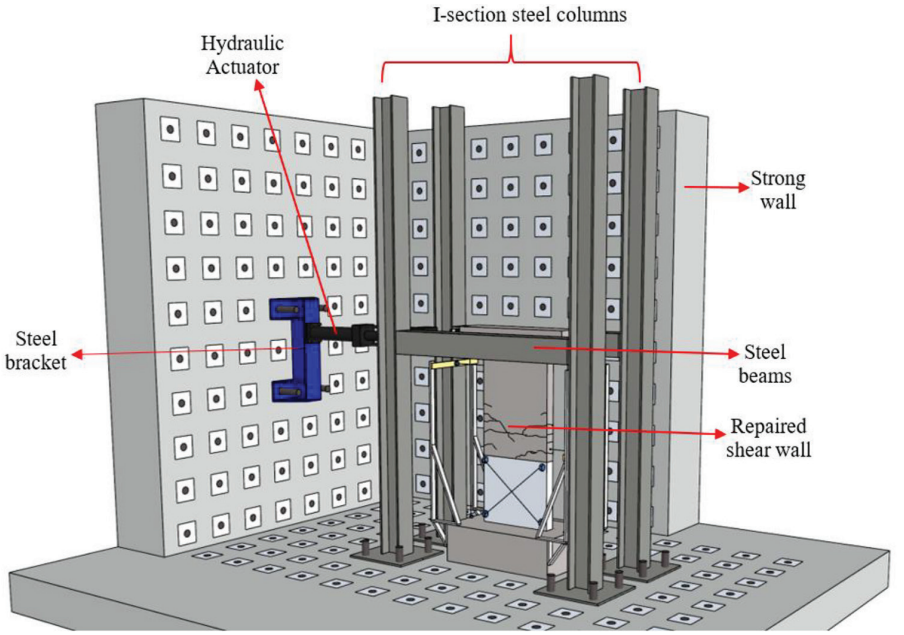

Fig. A2—Test setup assembly.

ARE YOU A RESEARCHER?

SIGN UP FOR ORCID TODAY!

ORCID provides a persistent digital identifier that distinguishes you from every other researcher and, through integration in key research workflows such as manuscript and grant submission, supports automated linkages between you and your professional activities, ensuring that your work is recognized.

Individuals may use ORCID services freely and it's as easy as **1-2-3**:

1. REGISTER
2. ADD YOUR INFO
3. USE YOUR ORCID ID

For more information and to register, visit:

WWW.ORCID.ORG

NEW Symposium Publications from ACI

SP-347: Recent Developments in High Strain Rate Mechanics and Impact Behavior of Concrete

This Symposium Volume reports on the latest developments in the field of high-strain-rate mechanics and behavior of concrete subject to impact loads. This effort supports the mission of ACI Committee 370, Blast and Impact Load Effects, to develop and disseminate information on the design of concrete structures subjected to impact, as well as blast and other short-duration dynamic loads.

Available in PDF format: $69.50
(ACI members: $39.00) ($30.50 savings)

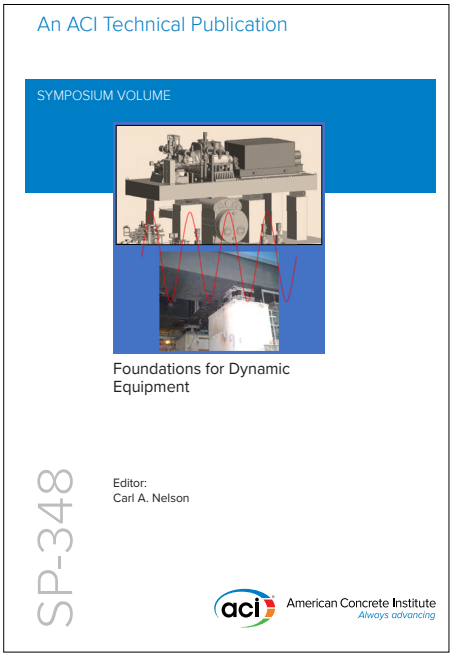

SP-348: Foundations for Dynamic Equipment

This special publication grew out of the Technical Session titled “Application of ACI 351-C Report on Dynamic Foundations,” held at the ACI Spring 2019 Convention in Québec City, Québec. Following this event, ACI Committee 351 decided to undertake a special publication with contributions from those session participants willing to develop their presentations into full-length papers. Three papers included in the current publication were contributed by these presenters and their coauthors, with six additional papers provided by others.

Available in PDF format: $69.50
(ACI members: $39.00) ($30.50 savings)

American Concrete Institute
+1.248.848.3700 • www.concrete.org